Schweizerischer Erdbebendienst
Service Sismologique Suisse
Servizio Sismico Svizzero
Swiss Seismological Service

ETH zürich

SITE CHARACTERIZATION REPORT
SRFW: Rheinfelden (AG), Werkhof

Paolo Bergamo, Donat Fäh

Last modification: 14.02.2020

Schweizerischer Erdbebendienst (SED)
Service Sismologique Suisse
Servizio Sismologico Svizzero
Servizi da Terratrembels Svizzer

ETH Zurich
Sonnegstrasse 5
8092 Zuerich
Schweiz
paolo.bergamo@sed.ethz.ch

Contents

Summary

The new SSMNet station SRFW was installed (06.06.2017) in the territory of the municipality of Rheinfelden (AG) about 1 km east of the city centre, between the municipal Werkhof and the Waldfiedhof. From a geological point of view, the station is located on a terrace composed of fluvio-glacial sediments ("Schotter") on the left bank of the Rhine (the river stretching approximately 800 m north of SRFW). Active seismic measurements, as well as a single-station noise recording survey, were performed to characterize the subsurface structure beneath the station. The site is characterized by a low fundamental frequency (0.65 Hz), which can be related to a deep interface between rock formations, well beyond the investigation depth reached by our measurements (which is approximately 80 m). The acquired H/V ratio curve presents as well two higher order peaks at 5.13 and 12.06 Hz, which can be assigned to a horizon at around 19 m depth (transition gravel terrace to weathered bedrock) and 4 m depth (surficial soil to gravel layers), respectively. The estimated V_{S30} value is 543 m/s, which classifies the site as B type soil according to both SIA261 (SIA, 2014) and Eurocode 8 (CEN, 2004).

1. Introduction.

In the framework of the second phase of the SSMNet (Swiss Strong Motion Network) renewal project, a new station, labelled as SRFW, was installed on 06.06.2017 in the territory of the municipality of Rheinfelden (AG) about 1 km east of the city center, between the municipal Werkhof and the Waldfriedhof (Figure 1). The host site is located on the southern bank of the Rhine (about 800 m away from the river) at an altitude of 300 meters above sea level. An active seismic survey and a single-station H/V_{noise} measurement were carried out on 14.05.2019 to ensure the seismic characterization of the site.

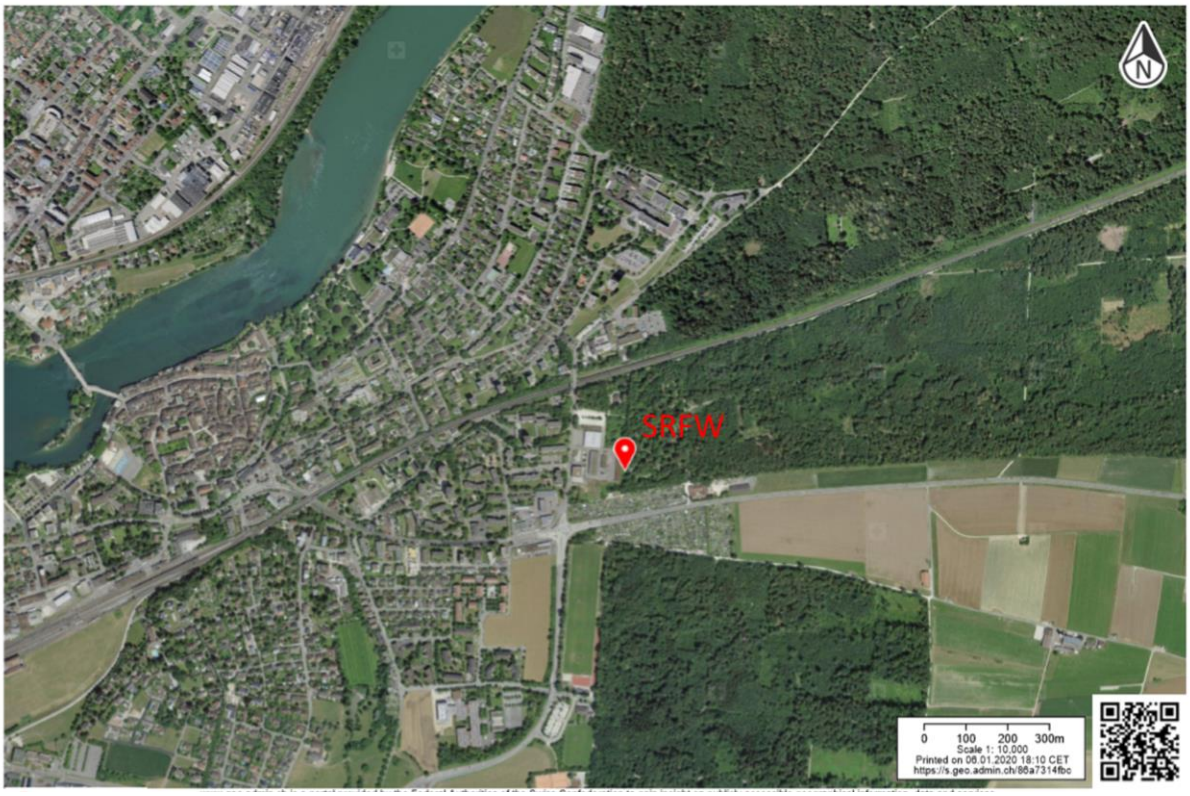

Figure 1 – Geographical location of SRFW, about 800 m south-east of Rhine river (© Swisstopo).

2. Geological setting

The site hosting SRFW is located on a lower terrace (Niederterrasse) formation of fluvioglacial sediments stretching on the southern bank of the Rhine (Figure 2). The formation dates to the late Pleistocene, and it overlies a Marls/Dolomite/Arenite bedrock which surfaces below the Rheinfelden city centre and deepens from West to East. The estimated depth to bedrock at SRFW is about 24 m, according to the bedrock model of Swisstopo (Swisstopo, 2019).

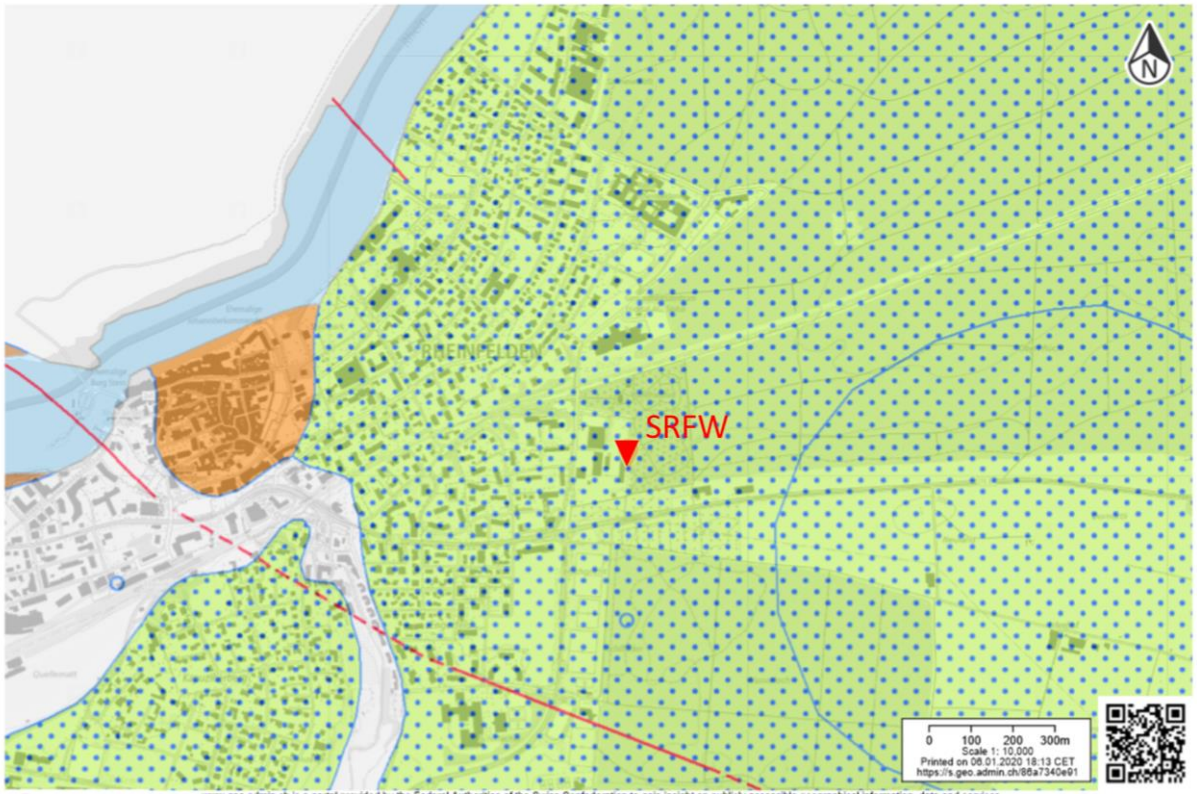

Figure 2 – Geological setting of SRFW location, as illustrated by the Swiss Geological Atlas 1:25000 (Sheet LK 1048, © Swisstopo). The station rests on a formation identified as lower terrace of fluvioglacial sediments dating to the late Pleistocene (light green with blue dots). Orange area = marls, dolomites, arenite; gray area = alluvial sediments; red lines = faults.

3. Active seismic measurements

The active seismic line was deployed close to SRFW, along a North-South direction (Figure 3).
For the sake of a comprehensive subsurface characterization, multichannel analysis of surface waves (MASW; Park et al., 1999) and P-wave refraction (Redpath, 1973) surveys were conducted.

3.1 Equipment

We used three sets of 8 three-component geophones (4.5 Hz corner frequency). Each geophone set was connected to a Geode datalogger; the three Geodes were coupled for time synchronization. The seismic source was a 5-kg sledgehammer, hitting a flat metal plate at seven source locations (red stars in Figure 3), as well as a wedge-shaped plate for Love wave excitation at the two shot points outside the geophone line. This plate is an isosceles right triangle: the hypotenuse is placed on the ground, and coupled to it with spikes penetrating the soil. The catheti are oriented orthogonally to the geophone spread, and alternately hit with the hammer.

The synchronization between the traces recorded by the geophones and the seismic source was ensured by a trigger device fastened to the hammer handle.

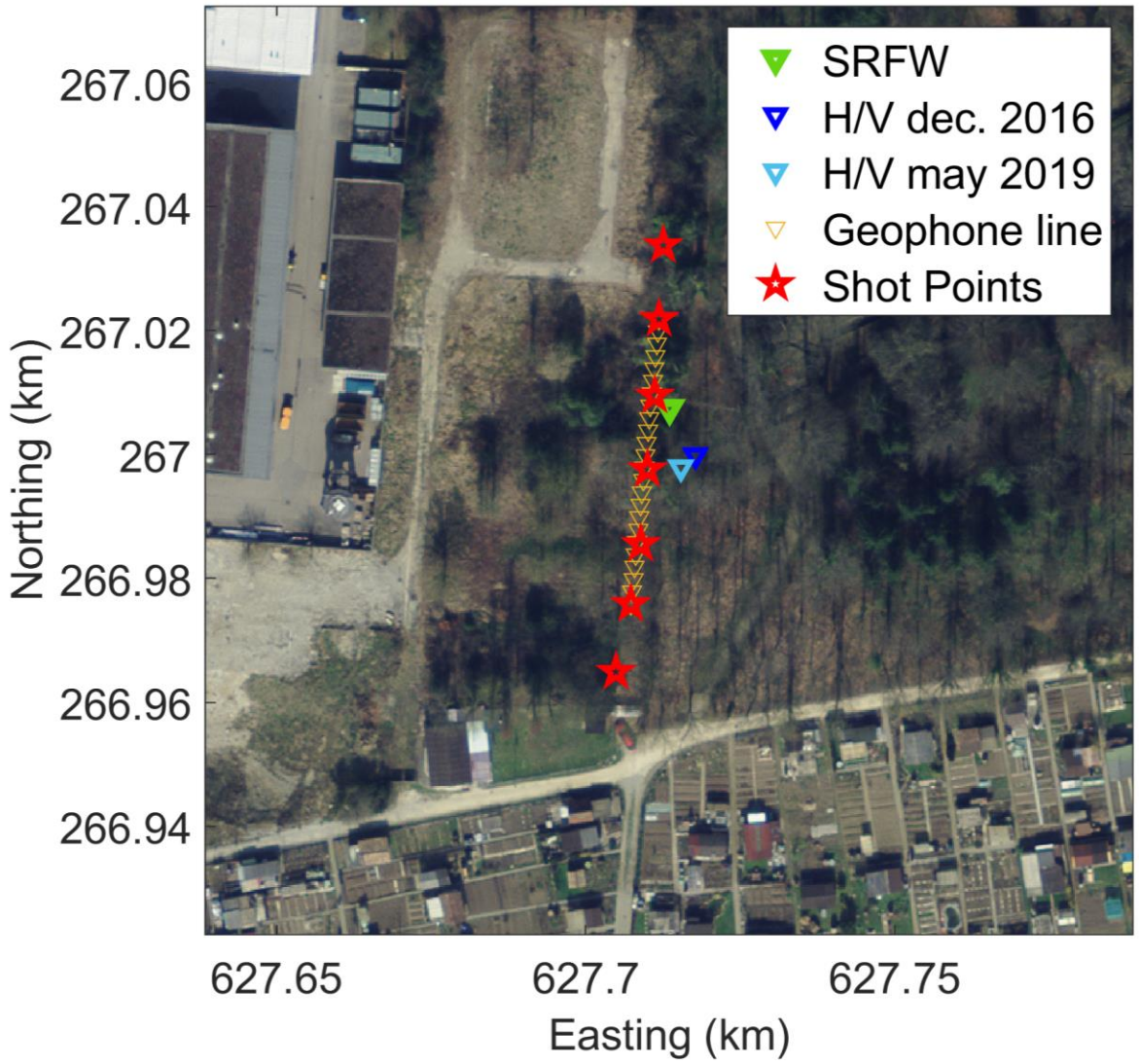

Figure 3 – Map representing the position of the targeted station (SRFW, green triangle), of the active seismic line (red stars – source and orange triangles - geophones) and of the noise recording sensors (blue and cyan traingles).

3.2 Geometry of the acquisition array

The seismic line was constituted by 24 three-component receivers aligned at regular intervals of 2 m, for a total length of 46 m. The geophones were laid on the soil with metal spikes ensuring a firm coupling with the ground.

As earlier anticipated, MASW and P-wave refraction measurements were performed. As for the refraction survey, the sources were placed at five locations along the receivers' line: at the south end, at 3 intermediate positions, and at the north end (Figure 3). At these shooting positions the sledgehammer was vertically blown on a flat metal plate. Two additional MASW shooting positions were placed south and north of the array, 12 m from the closest geophone (Figure 3); at these locations

we used both a wedge-shaped plate for Love waves excitation and flat plate for Rayleigh wave generation.

Figure 4 – Geophone array in place. The picture was taken near the north end of the line.

3.3 Acquisition

The time-sampling parameters adopted for both MASW and refraction acquisitions were the following: sampling interval = 125 µs, record length = 2 s, pre-trigger delay = -0.1 s.
At the seismic refraction source points, 10 hammer shots were blown; the traces generated by each blow were iteratively stacked and finally saved in a single *.sg2* file.
As for the Rayleigh wave acquisition, at each of the two shot points 15 hammer blows were repeated; the traces generated by each shot were separately saved in an *.sg2* file (without automatic stack).

For Love wave acquisition, at each shot point and at each of the two sides of the wedge plate 5 hammer shots were blown; the traces generated by each blow were iteratively stacked and finally saved in a single *.sg2* file.
In Figure 5 we show sample seismic sections from P-wave refraction (left), Rayleigh wave (center) and Love wave (right) shots (right).

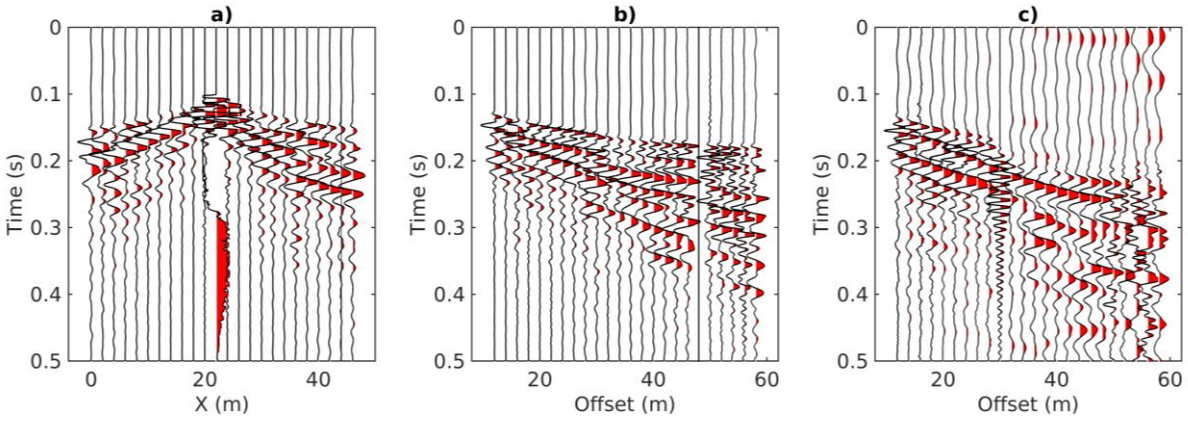

Figure 5 – Examples of acquired seismic sections. a) traces from a P-wave refraction shot (vertical component). The X coordinate is the distance from the southernmost geophone; b) traces from a Rayleigh wave shot (vertical component). The offset indicates the distance from the shooting position; c) traces from Love wave shots: the subplot displays the transverse-component traces obtained by subtracting the seismograms generated from the two opposite orientations of the source (i.e. hitting the two sides of the wedge-shaped plate). The offset indicates the distance from the shooting position.

3.4 Processing

3.4.1 Refraction processing

P-wave first-break arrival times were manually picked on the stacked seismograms representing the vertical component of soil surface vibration. For completeness, P-wave arrivals were picked on the seismic sections from all available source positions (therefore including also Rayleigh-wave shots). Figure 6 represents the travel-time curves, or hodocrones, obtained from each source position.

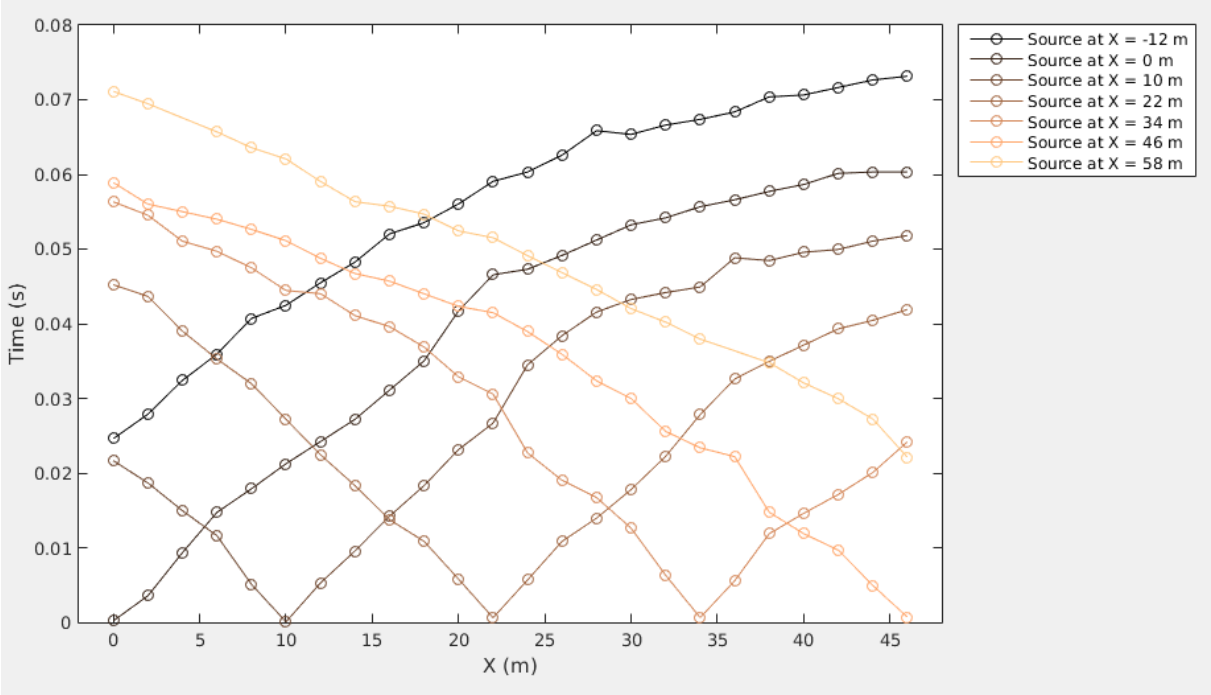

Figure 6 – P-wave refraction processing. Picked P-wave first-break arrival times from each shooting position. The X coordinate is the distance from the southernmost geophone.

3.4.2 Rayleigh wave data f-k processing

Rayleigh wave dispersion data were extracted from the vertical and radial component seismograms from MASW acquisitions. The considered seismic sections were processed by means of a 2D *f-k* (frequency – wavenumber) transform (Socco and Strobbia, 2004), in order to obtain a conversion of the recorded sets of traces from time–offset to frequency–wavenumber domain. *f-k* panels from single shot records with the same source position were summed to obtain spectral images with greater S/N ratio (O'Neill, 2003; Neducza, 2007). The energy maxima corresponding to the Rayleigh wave dispersion curves were picked on these stacked panels; spectral amplitude peaks from individual shot recordings were identified as well, and used to define the uncertainty intervals in the estimation of phase velocities (Socco et al., 2009; Boiero and Socco, 2010).

Figure 7 shows the stacked *f-k* panels from the considered seismic records, as well as the corresponding picked energy maxima. The dominant feature in all *f-k* spectra is a branch extending continuously in the 10-50 Hz frequency band, with wavenumbers between 0.1 and 1.5 rad/m. This feature is to be associated with the fundamental mode of Rayleigh wave propagation. At lower wavenumbers and higher frequencies other branches do exist and were picked. Their appearance is not necessarily coherent across all the four spectra, and they can be assigned to higher modes of Rayleigh wave propagation.

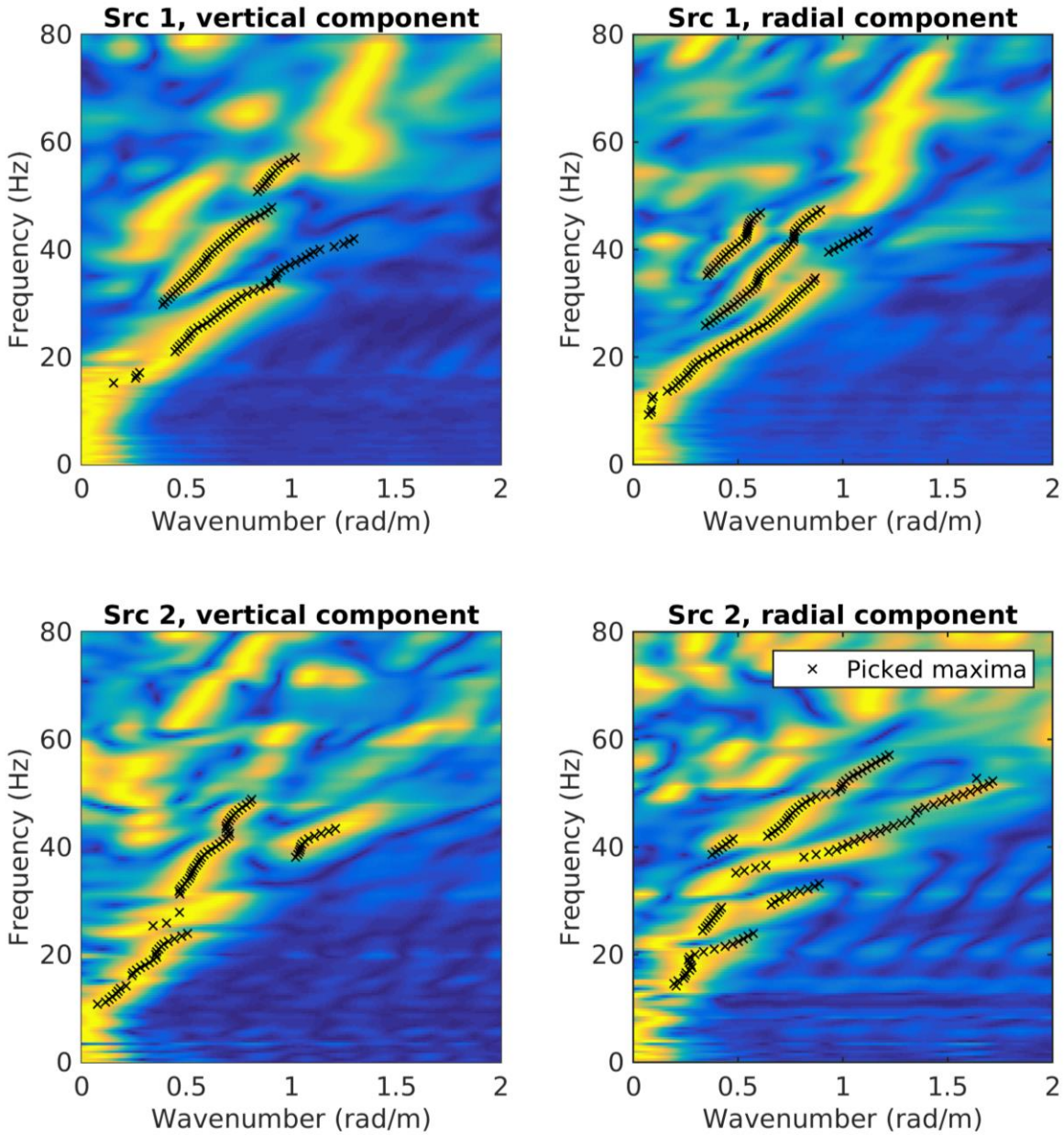

Figure 7 – Stacked normalized f-k spectra obtained from vertical and radial components of the seismic section with source positioned 12 m from the southernmost geophone (Src 1), or 12 m from the northernmost receiver (Src2). Black crosses are the picked energy maxima, corresponding to Rayleigh wave dispersion curve data points.

For a careful modal attribution of the picked branches we followed an approach inspired by the procedures proposed by Maraschini and Foti (2010) and Abdel Moati et al. (2013) and extensively described in the site characterization report of station SBIK (Bergamo et al., 2018).

The basic idea is to test the agreement between the experimental apparent dispersion curve and a set of synthetic curves corresponding to a vast population of possible subsurface models, assuming a priori only the reliable modal attribution of few data points, and letting the others free to be assigned to the closest (in terms of phase velocity) simulated mode. The synthetic curve that best "explains" (i.e. closely matches) all (or most of) the experimental data points, and therefore achieves the lowest misfit, is assumed to propose the most likely modal attribution.

The mode numbering resulting from this approach is shown in Figure 8. The fundamental mode of Rayleigh waves extends continuously across all the available frequency band (10 – 60 Hz) with velocities decreasing from 750 to 250 m/s. Above the fundamental mode sparser dispersive branches were attributed to 1st and 2nd higher modes. Finally, the four curves obtained from each MASW source points (north and south of the array) and each component of propagation (vertical and radial) were merged into a single curve, representative for SRFW site (Figure 18).

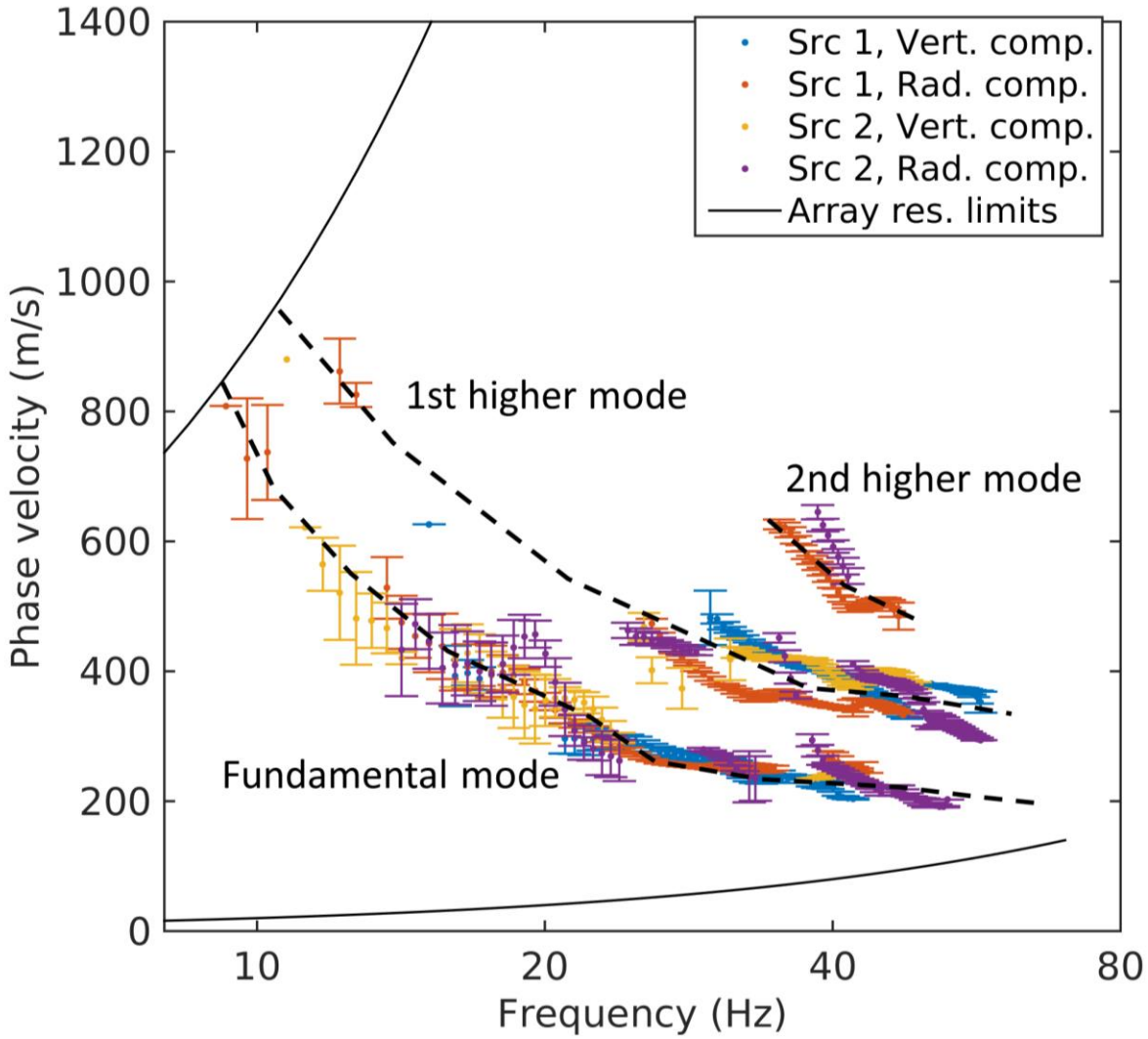

Figure 8 – Multimodal Rayleigh wave dispersion curves obtained from f-k processing (picked on the four stacked f-k panels of Figure 7). The modal identification is represented with a dashed black curve.

3.4.3 Love wave data f-k processing

The hammer blows exerted on the slant faces of the wedge apply a two-component excitation to the ground: a vertical and a horizontal component, the direction of the latter depending on which face of the plate the stroke is given. Therefore, by summing the seismic traces obtained hitting the wedge on the two sides, the effects of the horizontal components are mutually eliminated, while the vertical

components interact constructively; by computing the difference of the corresponding seismograms, the vertical components nullify each other, while the horizontal components interact constructively (Schmelzbach et al., 2016; Sollberger et al., 2016). Consequently, the sum operator is equivalent to the use of a vertical blow; the difference operator is equivalent to a pure shear source (suitable for the observation of Love waves). As example, the panel to the right in Figure 5 represents the section obtained by computing the difference of the transversal component traces acquired when using the wedge-shaped plate (hence this common shot gather corresponds to a solely SH excitation).

Therefore, for the extraction of Love wave dispersion data, 2D *f-k* analysis was applied to the seismograms obtained as difference between the transversal component traces acquired when alternately hitting the two opposite faces of the wedge-shaped plate.

Figure 9 shows the *f-k* panels obtained from the two shooting positions suitable for MASW (Love) analyses (north and south of the geophone line), as well as the picked energy maxima. The corresponding dispersion curves (Figure 10) comprise a fundamental mode extending from 10 to 55 Hz, with phase velocities decreasing from 600 to 250 m/s. The curve from shooting position 2 (north of the array) includes as well a relatively short branch identified as 1st higher mode.

Finally, the two curves were merged into a single one, representative for SRFW site (Figure 18).

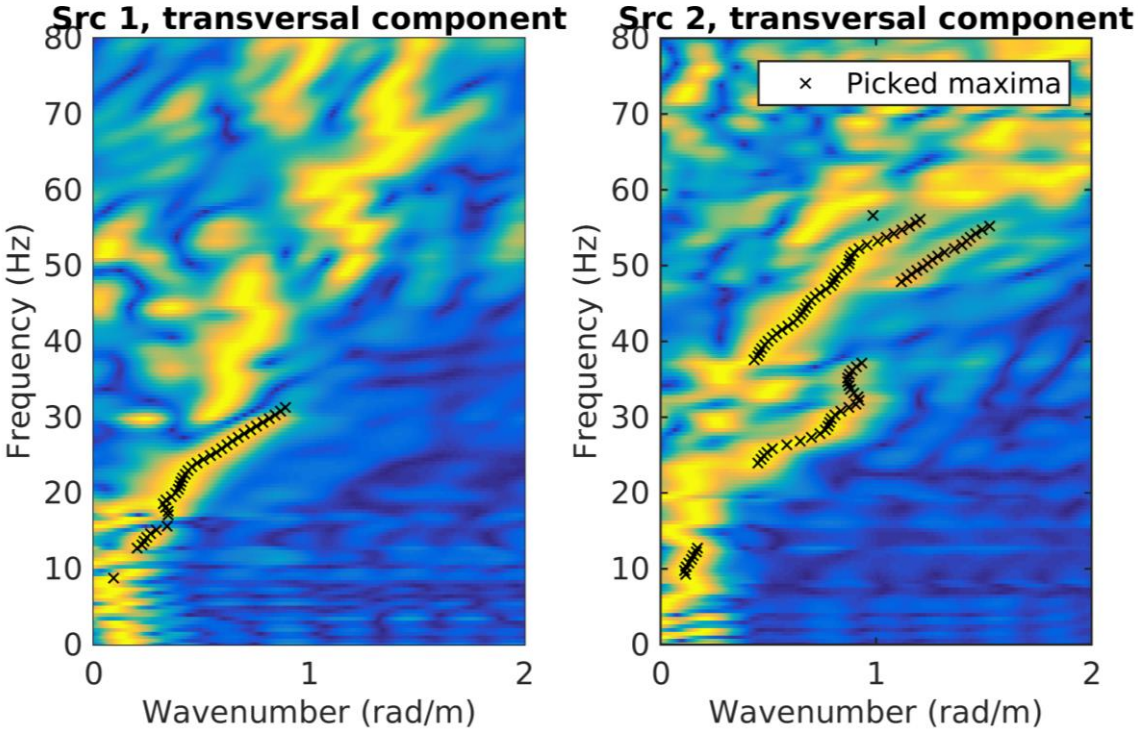

Figure 9 – Normalized f-k spectra obtained from the difference of the seismic sections (transversal component) produced by alternately hitting the two sides of the wedge-shaped plate; src1 is the shooting point 12 m south of the array, src2 is the shooting point 12 m north of the array. Black crosses are the picked energy maxima, corresponding to Love wave dispersion curve data points.

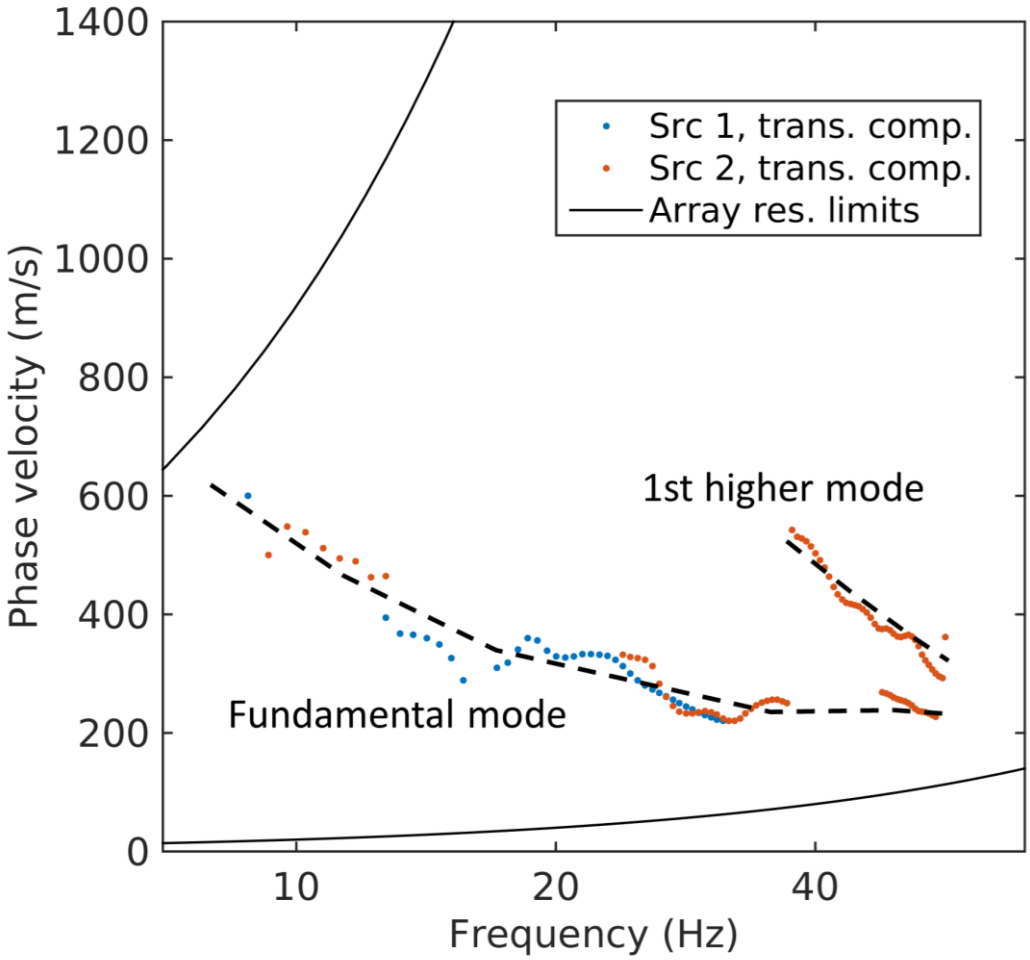

Figure 10 – Multimodal Love wave dispersion curves obtained from f-k processing (picked on the two f-k panels of Figure 9). The modal identification is represented with dashed black lines.

3.4.4 WaveDecActive

To retrieve the properties of Rayleigh wave propagation in terms of phase velocity and ellipticity the seismic traces acquired for the Rayleigh wave survey were also processed with the WaveDecActive code (Maranò et al., 2017). WaveDecActive implements a maximum likelihood algorithm for the analysis of Rayleigh waves generated by a controlled source. Key parameters required by WaveDecActive are the definition of the maximum number of Rayleigh waves that the code attempts to identify, and the value of parameter γ, which is able to modify the approach of the code towards wave identification from a Bayesian information criterion (γ=1) to a maximum likelihood approach (ML, γ=0) or a compromise between the two (0<γ<1). Following the recommendations of the code's author (Maranò, 2016) and some preliminary attempts, the maximum number of waves was set to 3 and γ to 0.2, thus opting for an approach close to a maximum likelihood solution.
The obtained results are displayed in Figure 11, showing the estimated Rayleigh wave phase velocities (left panel) and ellipticity angles (right panel) for the considered shots.

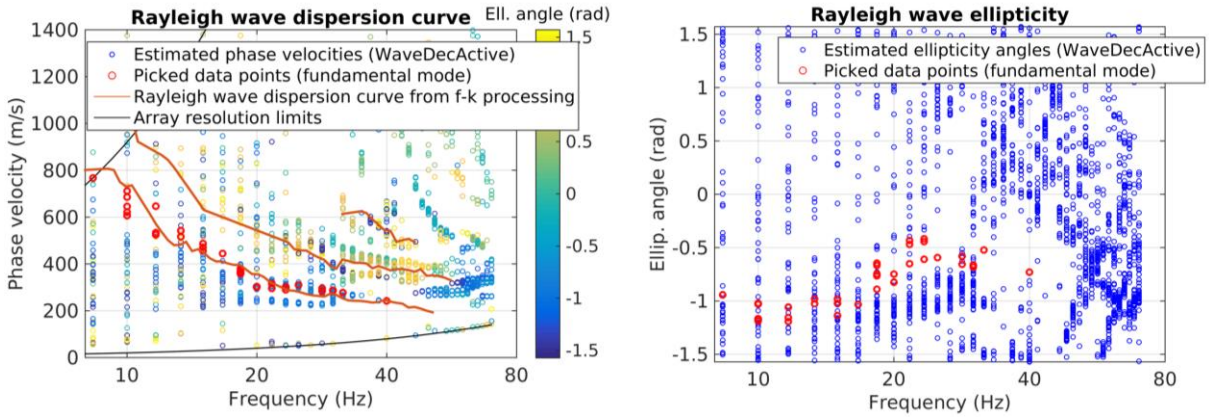

Figure 11 – Extraction of Rayleigh wave dispersion and ellipticity curve from WaveDecActive. Left: all estimated values of phase velocities (blue-to-yellow circles) and data points selected as belonging to the fundamental mode of Rayleigh wave propagation (red circles). Right: all estimated values of ellipticity angle (blue circles) and data points selected as belonging to the fundamental mode of Rayleigh wave propagation (red circles).

Despite the fact that we filtered out, at each frequency, all the estimates with amplitude below the 10th percentile of the overall population, the results seem anyway quite confused, with many, segmented dispersive events.
However, when superimposing the dispersion curve from f-k analysis (orange line in Figure 11, left panel), it is possible to identify two branches following approximately the fundamental and first higher mode. We picked the (negative) ellipticity angle estimates along the Rayleigh wave fundamental mode to obtain the corresponding ellipticity curve (Figure 11, right panel). Interestingly, the obtained curve joins quite well at around 10 Hz with the ellipticity curve derived processing with RayDec (Hobiger et al., 2009) the single-station passive recordings (see section 4 and Figure 18).

4 Passive seismic measurement

4.1 Acquisition and equipment

Besides active seismic surveys, a single-station noise recording measurement was performed on the same acquisition day. Unfortunately, the acquisition was not successful, due to unknown reasons (possibly a malfunctioning of the cable connecting the Lennartz 3C 5s seismometer to the Quanterra Q330 datalogger). Therefore, we resorted to an ambient vibration measurement from the SED H/V database (https://stations-intranet.ethz.ch/en/site-characterization) carried out in December 2016, during the phase of preliminary survey for the choice of location for the permanent station. The measurement was performed just 7 m south of SRFW (Figure 3); the sensor (Lennartz 3C 5s seismometer) was placed on a metal tripod in contact with the ground (Figure 12). The sampling frequency was 200 Hz and the recording spanned a 30-minute time interval; a Quanterra Q330 datalogger was employed.

Figure 12 – Single-station ambient vibration recording performed in December 2016.

4.2 Processing

The passive traces retrieved from the SED H/V database were re-processed with the aim of:

- estimating the H/V ratio of recorded noise, thus identifying the fundamental frequency of resonance of the site (Nakamura, 1989) by the use of classical H/V methods (as implemented in Geopsy software, www. geopsy.org; classical H/V of Fäh et al., 2001).
- estimating the ellipticity of Rayleigh wave as a function of frequency by resorting to refined algorithms (Raydec, Hobiger at al., 2009; time-frequency method, Poggi and Fäh, 2010; wavelet-based time-frequency method as implemented in Geopsy software).

To obtain a more reliable estimation of Rayleigh wave ellipticity the latter methods aim at eliminating the contributions of other waves besides Rayleigh waves when compared to the classical H/V technique.

The results are shown in Figure 13. All applied techniques yield similar H/V or ellipticity curves with three peaks at around 0.65, 5.1 and 12.1 Hz, separated by shallow troughs and reaching increasing values of H/V ratios (generally just below 2 for the 0.65 and 5.1 peaks, and just above 2 for the 12.1 peak).

We verified the absence of monochromatic noise sources related to human activities by visually inspecting the power spectrum of the three recorded components (Figure 14); no artefact can be identified in each of three subplots of Figure 14, hence our traces contain useful ambient noise across all the frequency spectrum.

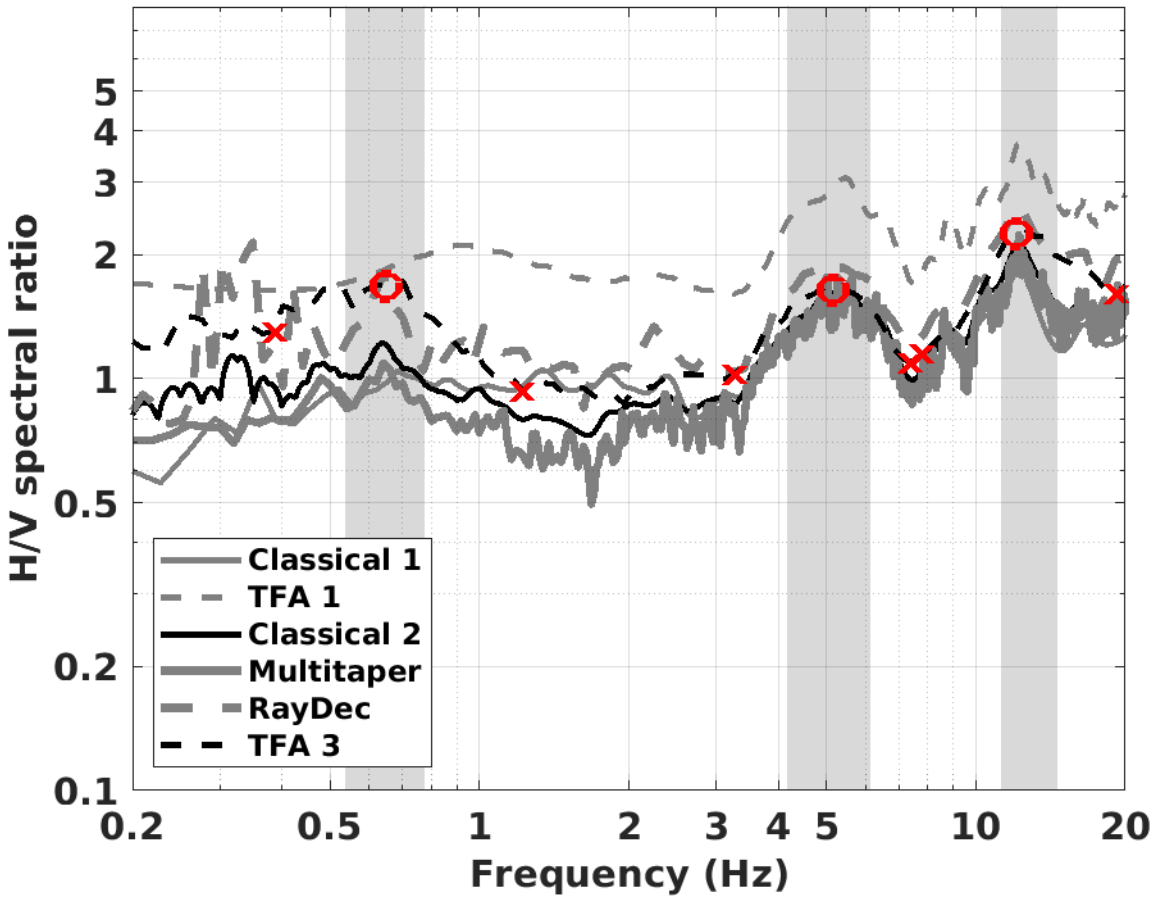

Figure 13 – H/V ratio and ellipticity curves obtained from the processing of noise recording data, using several algorithms. Classical 1: Geopsy; Classical 2: Fäh et al., 2001; TFA1: wavelet-based time-frequency method as implemented in Geopsy software; TFA3: time-frequency method, Poggi and Fäh, 2010; Raydec: Hobiger et al., 2009. Picked resonance frequencies are indicated by red circles; the corresponding intervals are marked by red crosses.

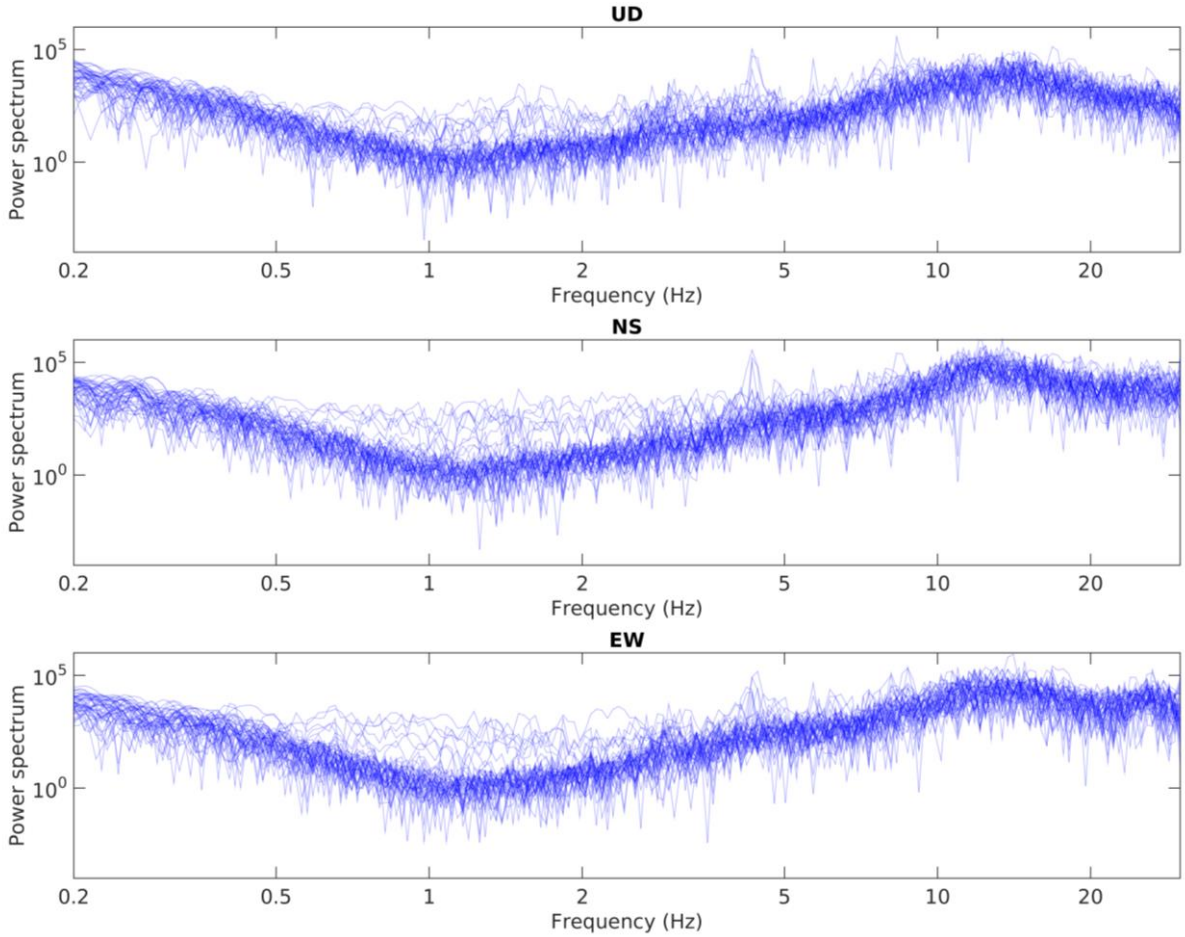

Figure 14 – Power spectra for each of the three components of recording for the passive measurement. Every thin blue line depicts the PSD of 30 seconds of recordings.

The recordings from the passive sensor were also processed with the polarization tool of Burjanek et al. (2010). In Figures 15 and 16 we display the produced ellipticity (as defined in Burjanek et al., 2010) and strike graphs as a function of frequency. The ellipticity plot (Figure 15) shows only minor troughs at ~5.1 and 12.1 Hz, which correspond to the H/V peaks in Figure 13. For the polar strike (Figure 16), no significant directionality effect can be identified, hence the SRFW site has no 2D or 3D resonance effects.

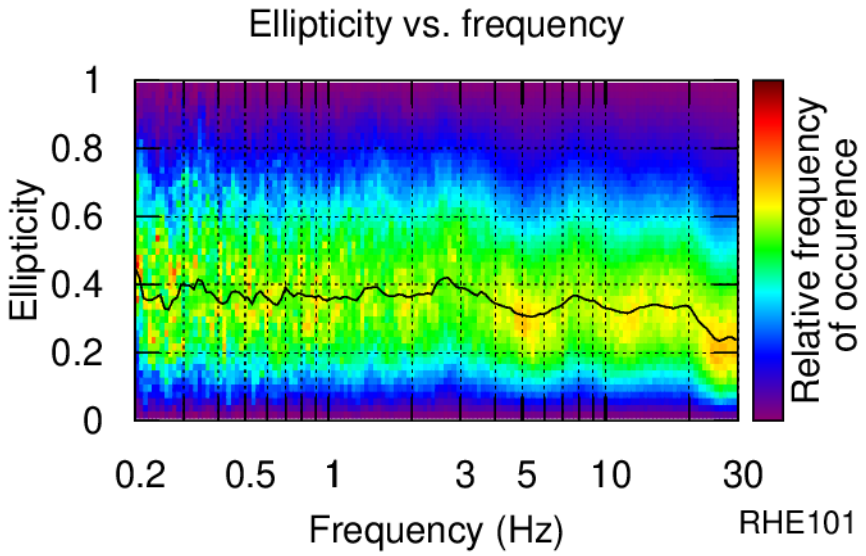

Figure 15 – Polarization analysis. Ellipticity vs frequency graph. The ellipticity is here intended as in Burjanek et al. (2010), i.e. the ratio between minor and major axes of the ellipse describing the instantaneous particle motion recorded at the soil surface.

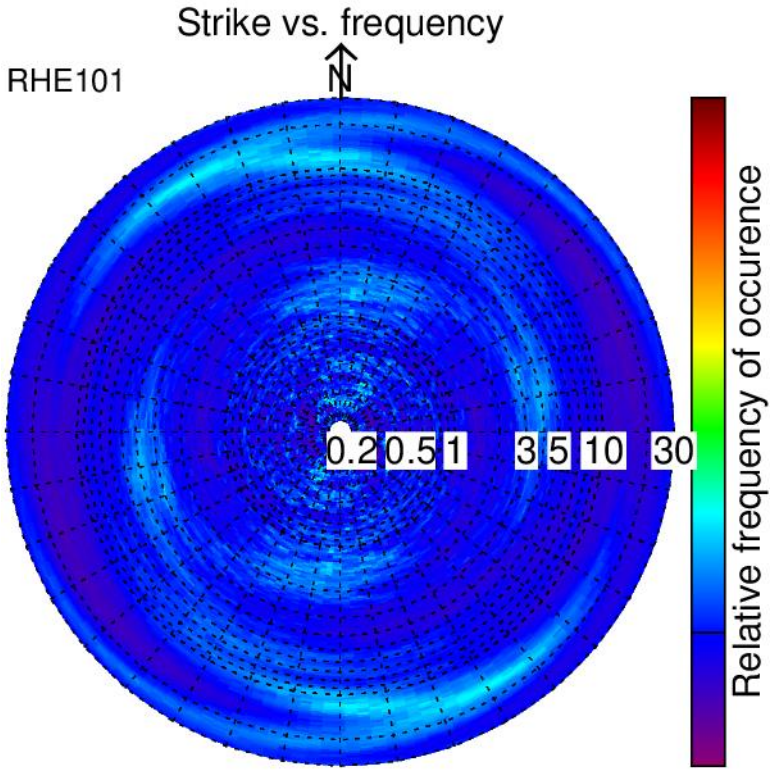

Figure 16 – Polarization analysis. Polar strike vs frequency graph.

5 P-wave travel-time inversion

A shallow V_P model of the subsurface was retrieved with the tomographic inversion of the picked P-wave arrival times (section 3.4.1). We used the seismic refraction tomography (SRT) inversion code developed at ETH Zurich by Lanz et al. (1998). The code performs a deterministic inversion of the arrival times. To minimize the distance between experimental and simulated arrival time a starting model is iteratively updated. For the inversion the 2D subsurface section below the active seismic array was modeled as a grid of 2 x 2 m cells. The initial model was defined as linear gradient of P-wave velocity with depth, increasing from 500 m/s at the surface to 2500 m/s at 22 m depth. A moderate constraint of spatial regularization was adopted.

The code converged to the final solution after 12 iterations, reaching a satisfactory fit with the experimental data (final RMSerror = 1.29 ms). From the analysis of the ray-paths at the last iteration it is evident that the portion of 2D section with a sufficient ray coverage (i.e. constrained by input data) is the central area just below the geophone spread. It covers a maximum depth of approximately 14 m. This portion of the 2D section is the final result of the inversion process (Figure 17).

As shown in Figure 17, at the center of the section the shallow 4 meters have a P-wave velocity around 525 m/s, increasing to 1000-1200 m/s at about 10 m depth. V_P appear to gradually increase towards the north end of the line.

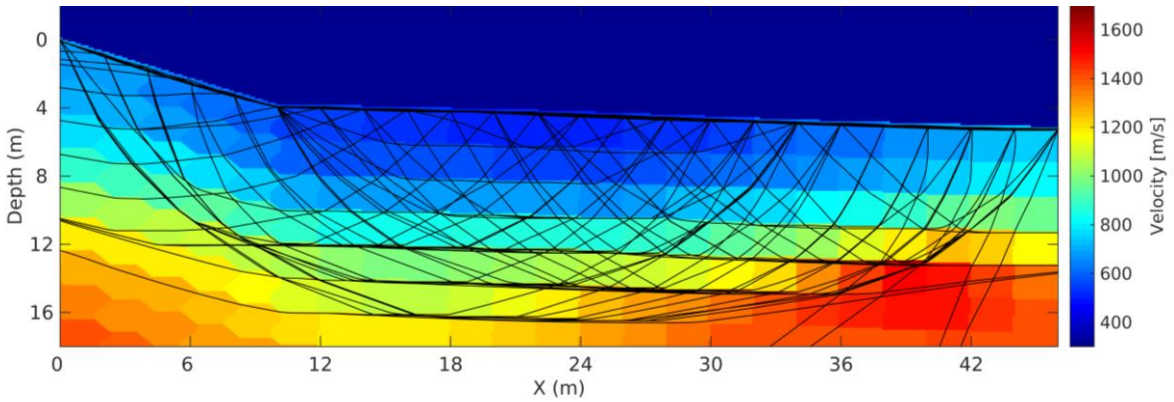

Figure 17 – tomographic inversion of P-wave first-break arrival times. 2D V_P section at the last iteration, with the superposition of the modeled ray paths (black lines). The X coordinate is the distance from the southernmost geophone.

6 Inversion of surface wave data

The Love and Rayleigh wave dispersion and ellipticity curves obtained from the processing of active and passive seismic data (see section 3.4) were inverted for the 1D S-wave velocity profile of the investigated site. For the inversion an ad-hoc code implemented in Matlab® was used. The code performs a Monte Carlo inversion, first generating a population of possible joint V_S/V_P profiles, then computing the synthetic curves corresponding to each model, and finally evaluating the misfit with

respect to the experimental curves. For the solution of the forward problem we resorted to Hermann (2013).

6.1 Inversion target

The target we selected for the inversion consists of:

- The multimodal Rayleigh wave dispersion curve, as obtained from the processing of active data with the f-k processing (section 3.4.2; see Figure 18, top left).
- The multimodal Love wave dispersion curve, as obtained from the processing of active data with the f-k processing (section 3.4.3; see Figure 18, bottom left).
- The Rayleigh wave ellipticity curve for the fundamental mode from the processing of active data with WaveDecActive code (section 3.4.4), translated from ellipticity angle (Figure 11) to the ratio between horizontal and vertical component of particle motion (ellipticity). At low frequency (< 10 Hz), this curve was joined with the ellipticity curve obtained from the single-station passive recording processed with Raydec (see section 4.2). This curve was attributed to the fundamental mode of Rayleigh wave propagation. To include the ~5.1 Hz peak we used data points from 10 down to 2.5 Hz for the inversion. The portion below 2.5 Hz was discarded as it is not accompanied by any information about surface wave phase velocity (the dispersion curves extend down to 8-10 Hz).

The phase velocity and ellipticity curves were resampled on a logarithmically-spaced frequency vector with 100 elements between 2.5 and 60 Hz.

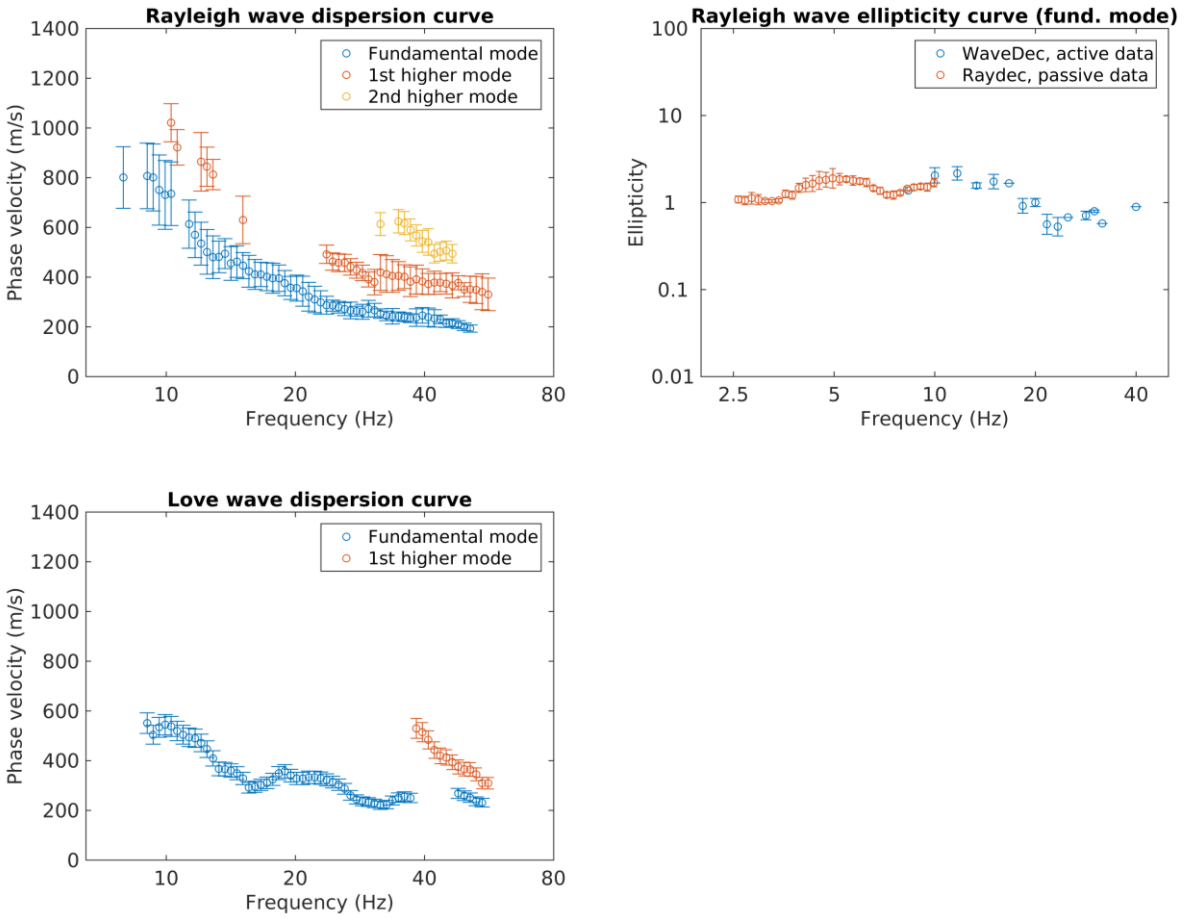

Figure 18 – Target of the Rayleigh wave data inversion process. Left: multimodal Rayleigh wave dispersion curve obtained from the processing of active data with f-k processing (top) and multimodal Love wave dispersion curve obtained from the processing of active data with f-k processing (bottom). Right: ellipticity curve for the fundamental mode of Rayleigh wave; the low-frequency portion was obtained by processing passive data with Raydec code; the high-frequency portion was obtained from the processing of active data with Wavedec code.

6.2 Parameterization of the model space

For the parameterization of the subsurface model two different strategies were followed: the soil column was modelled as a stack of either 6 or 5 homogeneous layers with variable thickness overlying an halfspace. In both parameterizations at each layer the V_S can vary within broad Monte Carlo boundaries. The same applies to V_P, although the resulting V_S/V_P ratio must be compatible with a range of possible values of Poisson's ratios set for each layer: 0.2 – 0.4 for the three shallowest formations (probably not water saturated, as indicated by SRT results), 0.2 – 0.49 for the following intermediate layers (to allow for the presence of water-saturated materials), and 0.2 – 0.35 for the lower halfspace. Bulk density values are attributed to each layer increasing from 1.9 t/m^3 for the weathering formation to 2.25 t/m^3 for the halfspace. For the three deepest layers S-wave velocity values are forced to be larger than that of the formation above.
For each parameterization we completed an inversion run with 1.5 10^6 randomly generated models.

6.3 Inversion results

In Figures 19-20 and 21-22 we show the results obtained from each of the two inversion runs: Figure 19-20 for the 6 layers + halfspace parameterization, and Figures 21-22 for the 5 layers + halfspace parameterization. The 5-layer parametrization yields slightly lower misfit values (minimum RMSE = 1.40, compared to RMSE = 1.42 for the 6-layer models), however the velocity profiles are generally consistent. The data fit is reasonably good for both surface wave dispersion and ellipticity curves.

As it is not possible to decidedly opt in favor of one parameterization against the other, we consider as final inversion result the 20 best performing (lowest RMSe) models, drawn from both subsurface modeling (maximum RMSe = 1.5; Figure 22).

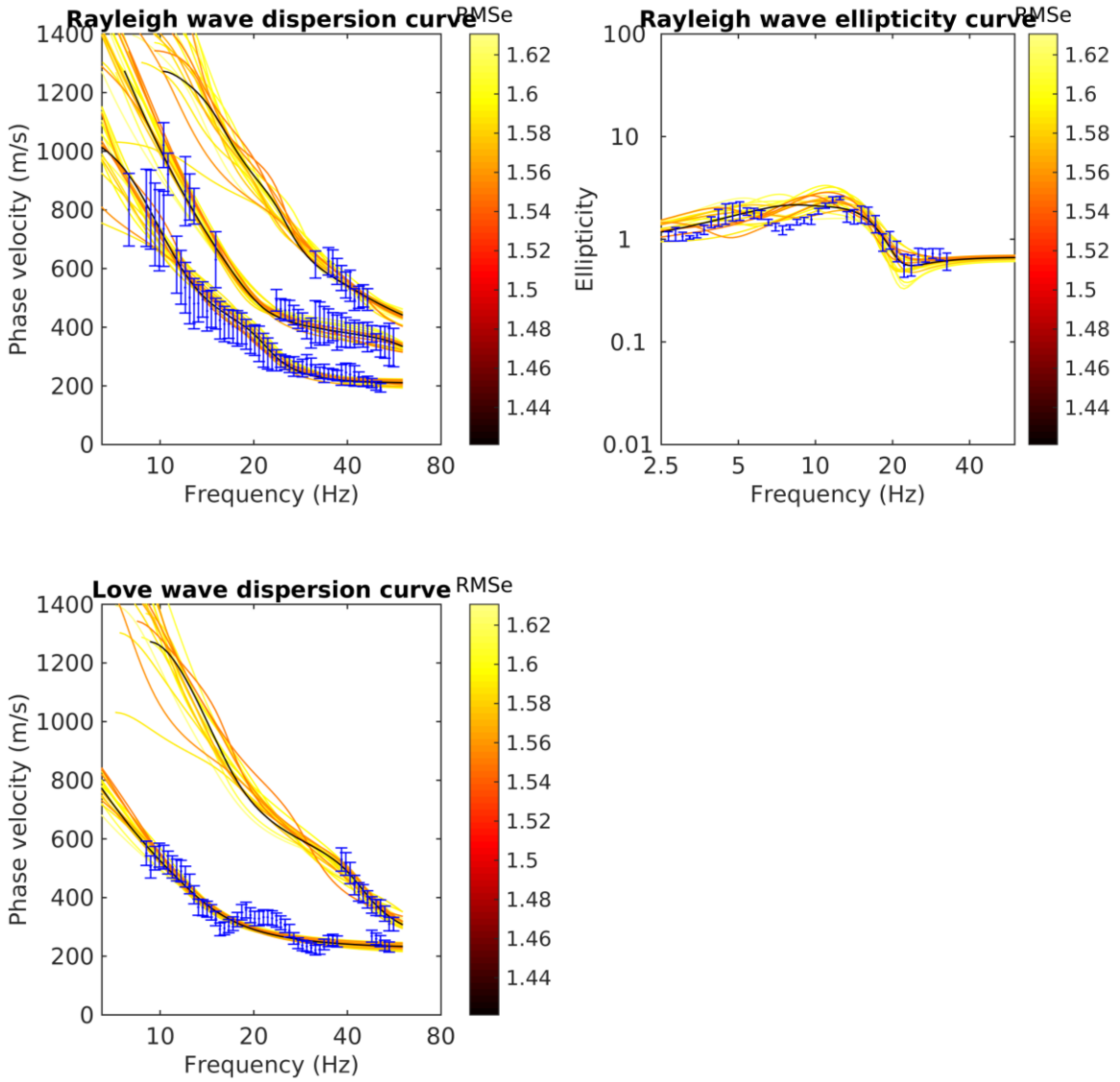

Figure 19 – Data fit (simulated vs experimental curves) for the 20 best performing models obtained from the 6-layer parameterization inversion run.

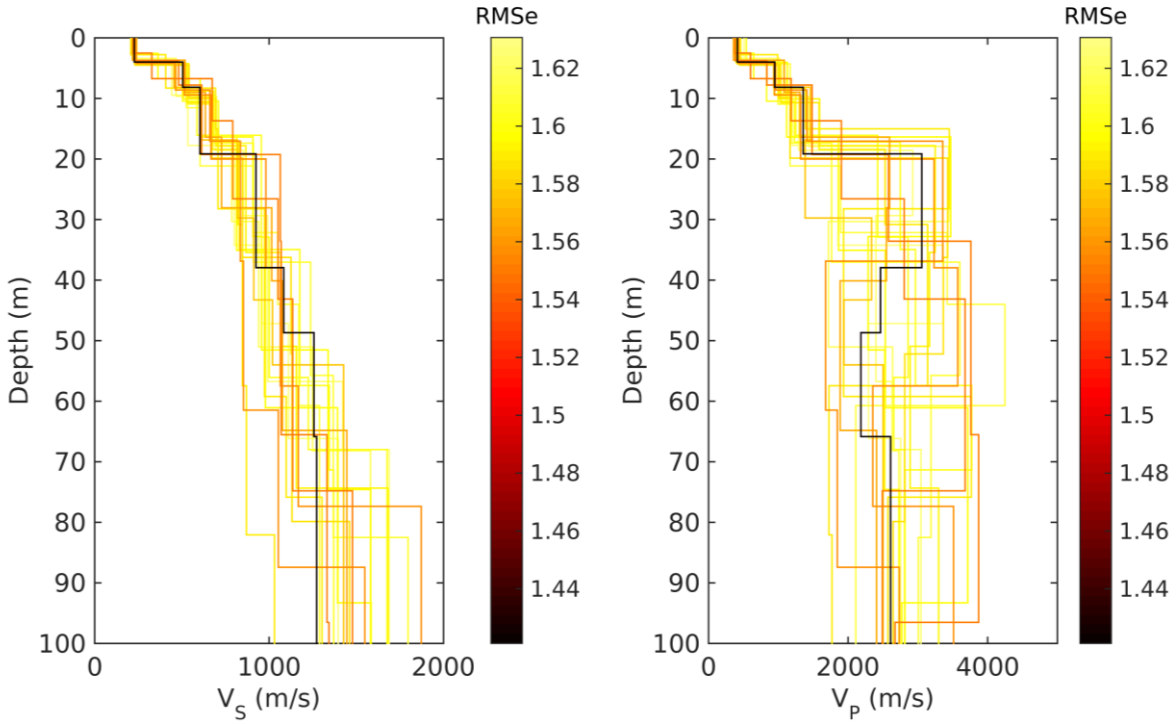

Figure 20 – 20 best performing velocity models obtained from the 6-layer parameterization inversion run.

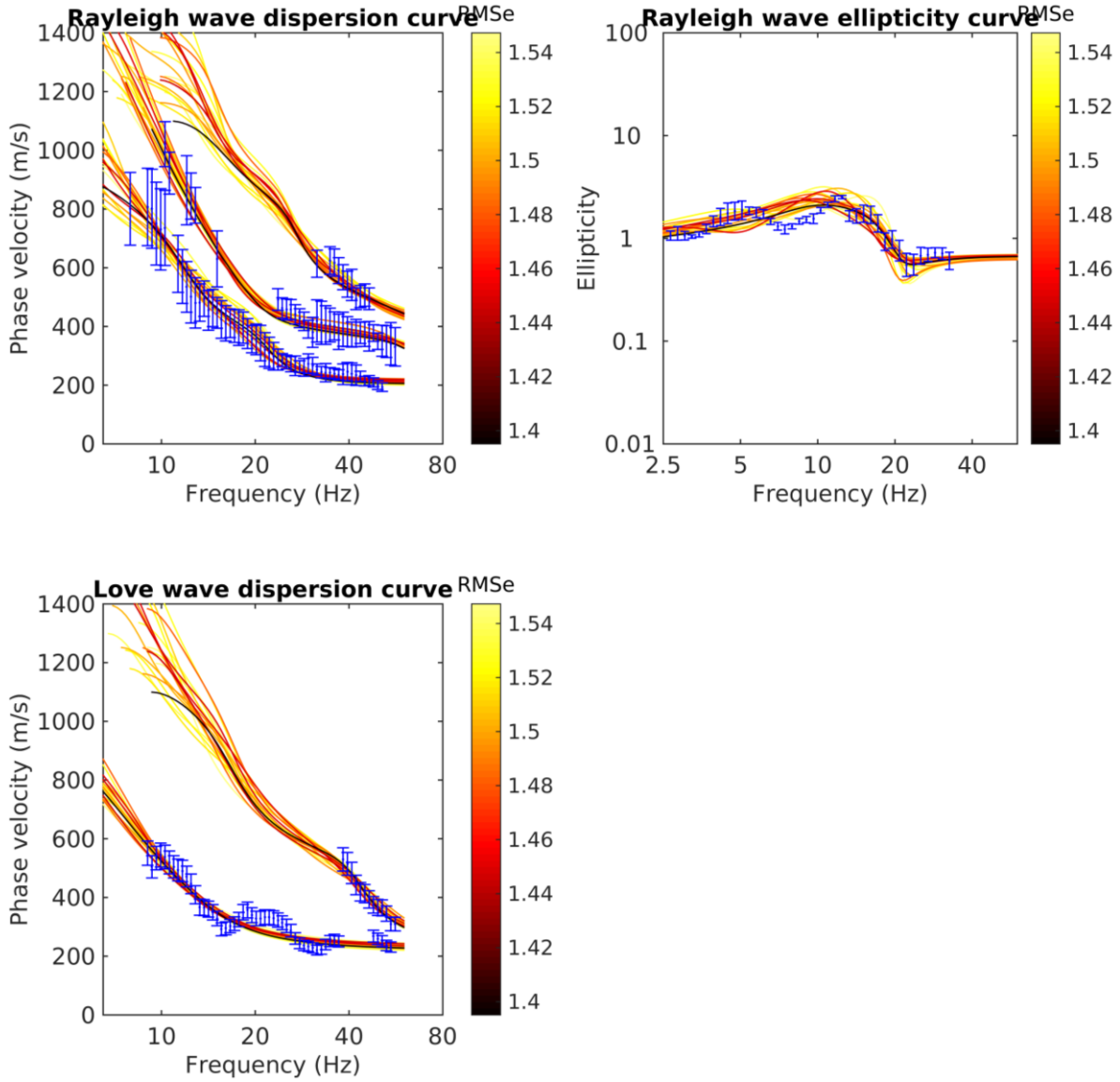

Figure 21 – Data fit (simulated vs experimental curves) for the 20 best performing models obtained from the 5-layer parameterization inversion run.

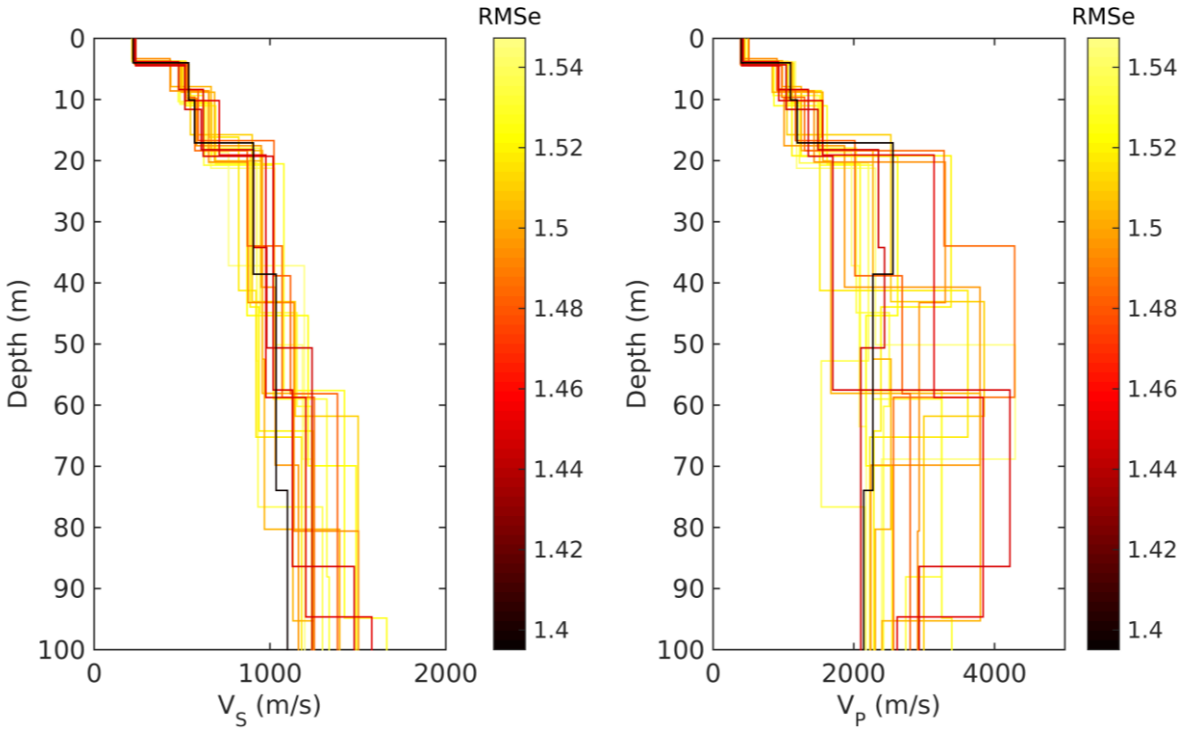

Figure 21 – 20 best performing velocity models obtained from the 6-layer parameterization inversion run.

7 Interpretation of the velocity profiles

7.1 Velocity profiles

The 20 best performing (i.e. lowest misfit) models from either the 6- or 5-layer parametrization inversions are considered as final result (Figure 22).

The upper 4 m have a V_S around 225 m/s, and they are presumably composed of weathering soil. Below, we meet two layers, with thicknesses of around 6 and 10 m, and S-wave velocity increasing from 500 to 650 m/s; these layers should correspond to the terrace formation indicated by the geological map (Figure 2). In the same depth range (0 – 20 m), we notice that the estimated V_P from surface wave data inversion agree with the velocities obtained from refraction tomography (red line in Figure 22, right panel).

At a depth of ~19 m depth, S-wave velocity sharply increases to about 950 m/s; this threshold probably indicates the transition between the gravelly "Schotter" and the Marls/Dolomite/Arenite bedrock below (quite likely degraded, hence the relatively low velocity). It should be noted that the sediments-to-bedrock model developed by Swisstopo for most of the Swiss territory (Swisstopo, 2019), indicates a bedrock depth of around 24 m at SRFW. Beneath the gravel-to-bedrock interface, the velocity of the rock gradually increases reaching V_S between 1100 - 1500 m/s at 80-90 m depth (approximately the investigation depth enabled by acquired data).

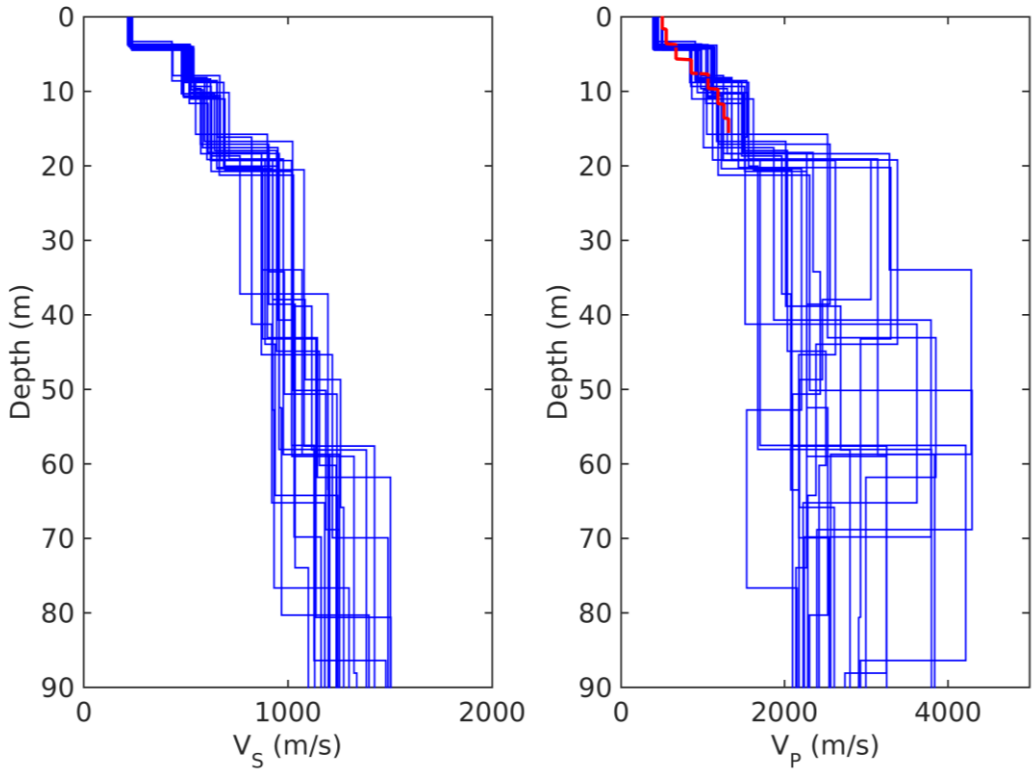

Figure 22 – Obtained V_S and V_P profiles. In the right panel the P-wave velocities at the midpoint of the retrieved SRT section (Figure 14) are shown (red line).

7.2 Quarter-wavelength representation

The quarter-wavelength velocity representation (V_S^{QWL}; Joyner et al., 1981) attributes the average velocity at a depth equal to ¼ of the corresponding wavelength to each frequency. V_S^{QWL} can be used as direct proxy for the local site characterization, as it physically relates the resolution on ground parameters with the characteristics of the propagating wave-field at the discrete frequencies. The derived quarter-wavelength impedance contrast (IC^{QWL}; Poggi et al., 2012) is the ratio between two quarter-wavelength average velocities from the top and bottom part of the velocity profile at a given frequency. It is a powerful tool to assess the influence of resonance phenomena in soft sediment sites. Figure 23 shows the average (over the population of the selected 20 best subsurface models) quarter-wavelength velocity (Figure 23 centre) and impedance contrast (Figure 23 bottom) representations. The obtained Vs30 (which is the average velocity corresponding to a quarter-wavelength of 30 m) is 543 m/s.

The IC^{QWL} graph shows one broad peak at 7 Hz (which can be associated with the impedance contrast between unconsolidated sediments and bedrock at 19 m depth, Figure 122, as well as sharp peak at 14 Hz (corresponding to the shallow interface at 4 m between soil and gravel).

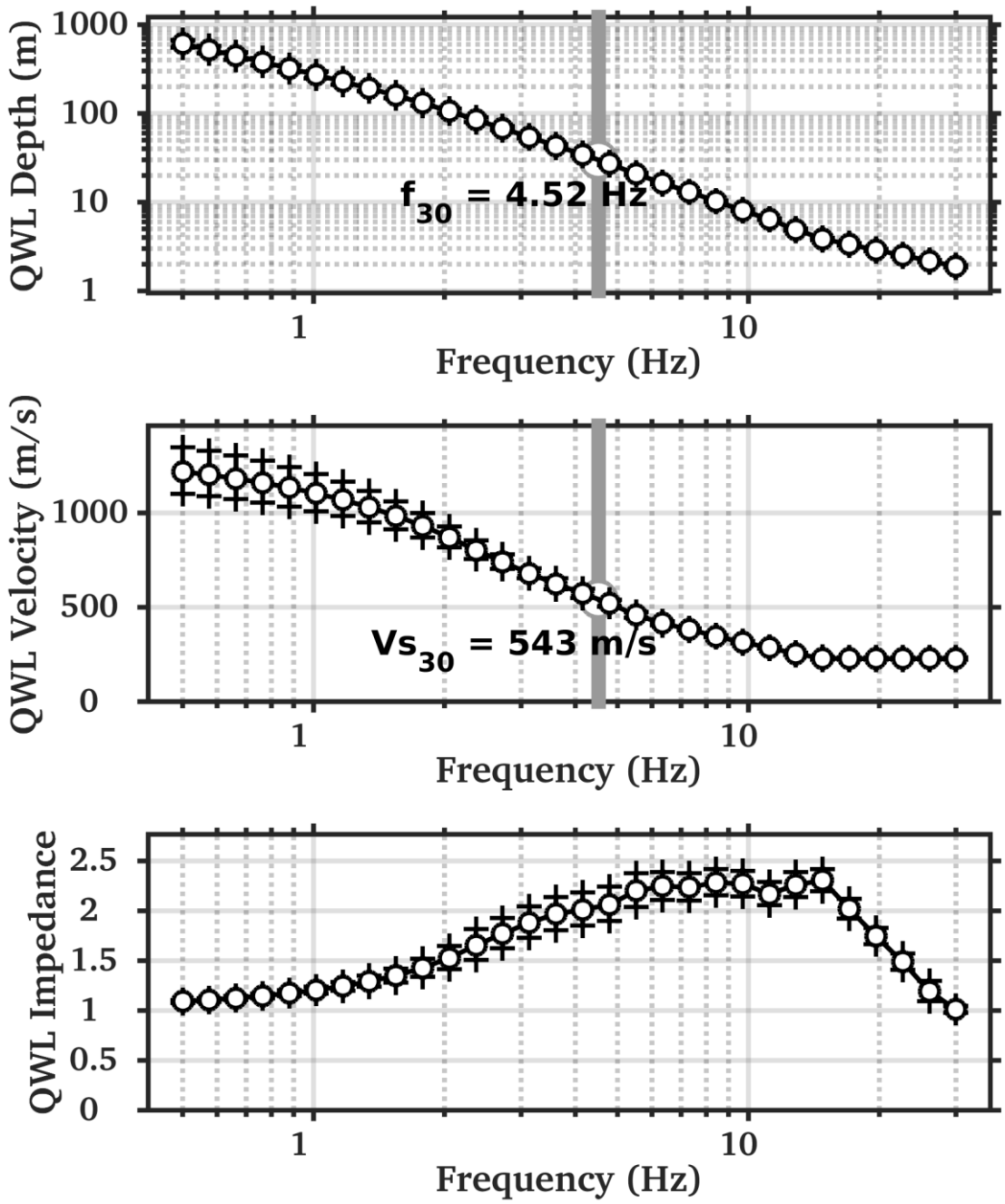

Figure 23 – Average quarter-wavelength representation of the selected velocity profiles (Figure 22). Top: depth; center: velocity; bottom: impedance contrast. The gray line in the top and center panel refers to Vs_{30}.

7.3 Amplification function

The theoretical SH-wave transfer function for vertical propagation (Roesset, 1970) was computed for each of the selected models (Figure 24). The transfer functions were then corrected for the Swiss reference rock model (Poggi et al., 2011).

These theoretical amplification functions (blue lines in Figure 24) are compared with the empirical amplification function obtained from spectral modeling (ESM; Edwards et al., 2013) of the SRFW recordings. The latter relies only on 7 events in the 1.25 – 10 Hz frequency band, and even fewer earthquakes at lower and higher frequencies (as of 16.01.2020). The empirical function is characterized by a frequency band between 2.5 – 6 Hz with amplification factors reaching 1.5 – 1.6, and a sharper peak at ~12 Hz. The first feature is mimicked by a wide hump present in all simulated curves, whose peak is comprised between 3.5 – 5.5 Hz; the feature is to be related to the interface between gravel and bedrock at approximately 20 m depth. As for the 12 Hz peak, the synthetic functions tend to place it at slightly lower frequencies (around 10 Hz). This feature is caused by the impedance contrast between surficial soil (225 m/s) and the stiffer gravel (500 m/s) below.

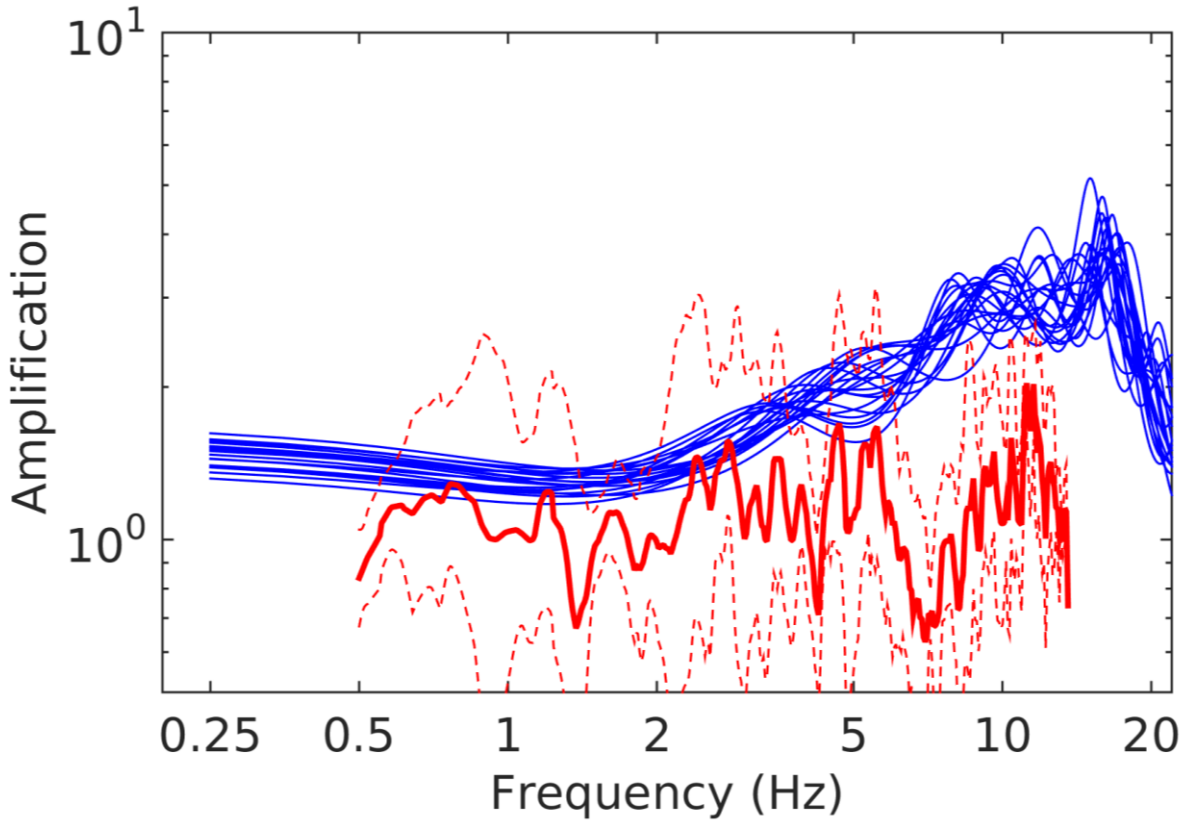

Figure 24 – Theoretical amplification functions (blue lines) from the selected velocity profiles corrected for the Swiss reference rock model and compared with the empirical amplification function for SRFW (red line, uncertainty intervals in red dashed line).

8 Conclusions

Active seismic measurements and a single-station noise recording were performed to characterize the structure of the subsurface below the SSMNet station SRFW (Rheinfelden, AG). Active data were processed to derive Rayleigh and Love wave dispersion, ellipticity (Rayleigh-only) curves, and to identify the first-break arrivals of P-waves (later inverted with a tomographic approach). Passive data were analyzed to estimate the ellipticity curve of Rayleigh waves. Love and Rayleigh wave dispersion and ellipticity curves were inverted for the S-wave velocity profile at the station location.

The upper 4 m have a V_S around 225 m/s, and they are presumably composed of weathering soil. Below, we meet two layers, with thicknesses of around 6 and 10 m, and S-wave velocity increasing from 500 to 650 m/s; these layers should correspond to the terrace formation indicated by the local geological map. At a depth of ~19 m depth, S-wave velocity sharply increases to about 950 m/s; this threshold probably indicates the transition between the gravelly "Schotter" and the Marls/Dolomite/Arenite bedrock below (quite likely degraded, hence the relatively low velocity). Beneath the gravel-to-bedrock interface, the velocity of the rock gradually increases reaching V_S between 1100 - 1500 m/s at 80-90 m depth (approximately the investigation depth enabled by acquired data).
The velocity contrasts at 4 (soil-to-gravel) and 19 (gravel-to-bedrock) m depth are responsible for the peaks at 12.1 and 5.1 Hz identified on the H/V curve. The fundamental frequency of 0.65 Hz is to be ascribed to a rock-to-rock contrast well below the maximum investigation depth.
The estimated V_{S30} value is 543 m/s, which classifies the site as B type soils according to both SIA261 (SIA, 2014) and Eurocode 8 (CEN, 2004). The engineering bedrock (H800) is at approximately 19 m depth.

References

Abdel Moati W.H., D. Boiero, and L.V. Socco, 2013. A tool for fast underground characterization for trenchless pipeline construction by horizontal directional drilling technology. 11th Offshore Mediterranean Conference and Exhibition, Ravenna, Italy, March 20-22 2013.

Bergamo P., M. Hobiger and D. Fäh, 2018. Site characterization report, SBIK – Biel/Bienne (BE), Kongresshaus/Palais des Congrès. Swiss seismological service (SED)

Boiero, D., and L. V. Socco, 2010. Retrieving lateral variations from surface wave dispersion curves analysis: Geophysical Prospecting, **58**, 977–996

Burjanek J., G. Gassner-Stamm, V. Poggi, J.R. Moore and D. Fäh, 2010. Ambient vibration analysis of an unstable mountain slope, GJI, 180, 820-828.

CEN, 2004. Eurocode 8: Design of structures for earthquake resistance – Part 1: general rules, seismic actions and rules for buildings. European Committee for Standardization, en 1998-1 edition.

Edwards, B., Michel, C., Poggi, V., and Fäh, D., 2013. Determination of Site Amplification from Regional Seismicity: Application to the Swiss National Seismic Networks. Seismological Research Letters, 84(4).

Fäh, D., F. Kind, and D. Giardini, 2001. A theoretical investigation of average H/V ratios. GJI, 145, no. 2, 535-549.

Herrmann, R. B., 2013. Computer programs in seismology: An evolving tool for instruction and research, Seism. Res. Lettr. **84**, 1081-1088, doi:10.1785/0220110096

Hobiger, M., P.-Y. Bard, C. Cornou, and N. Le Bihan, 2009. Single station determination of Rayleigh wave ellipticity by using the random decrement technique (Raydec). GRL, 36, L14303

Joyner, W. B., Warrick, R. E., and Fumal, T. E., 1981. The effect of Quaternary alluvium on strong ground motion in the Coyote Lake, California, earthquake of 1979. Bulletin of the Seismological Society of America, 71(4):1333–1349.

Lanz E., H. Maurer and A. G. Green, 1998. Refraction tomography over a buried waste disposal site. Geophysics, 63 (4), 1414-1433.

Marano' S., 2016. http://mercalli.ethz.ch/~marra/WaveDec/userguide_WaveDec.html

Marano, S., Hobiger M., P. Bergamo and D. Fäh, 2017. Analysis of Rayleigh Waves with Circular Wavefront: a Maximum Likelihood Approach. GJI, 210, 1570-1580.

Maraschini M., and S. Foti, 2010. A Monte Carlo multimodal inversion of surface waves. GJI, 182 (3). 1557 – 1566.

Nakamura, Y., 1989. A Method for Dynamic Characteristics Estimation of Subsurface Using Microtremor on the Ground Surface. Quarterly Report of RTRI, vol. 30, no. 1, 25- 33.

Neducza, B., 2007, Stacking of surface waves: Geophysics, 72, 51–58.

O'Neill, A., 2003, Full-waveform reflectivity for modelling, inversion and appraisal of seismic surface wave dispersion in shallow site investigations: PhD thesis, University of Western Australia, Perth, Australia.

Park, C. B., R. D. Miller, and J. Xia, 1999. Multichannel analysis of surface waves: Geophysics, **64**, 800–808.

Poggi, V., B. Edwards and D. Fäh, 2011. Derivation of a Reference Shear-Wave Velocity model from Empirical Site Amplification. BSSA, 101, no. 1, pp. 258-274

Poggi, V., B. Edwards and D. Fäh, 2012. The quarter-wavelength average velocity: a review of some past and recent application developments. 15th WCEE, Lisbon 2012.

Poggi, V., and D. Fäh, 2010. Estimating Rayleigh wave particle motion from three component array analysis of ambient vibrations. GJI, 180, no. 1, 251-267.

Redpath, B. B., 1973. Seismic refraction exploration for engineering site investigations: National Technical Information Service, Technical Report E-73-4.

Roesset, J. (1970). Fundamentals of soil amplification. In Hansen, R. J., editor, Seismic Design for Nuclear Power Plants, pages 183–244. M.I.T. Press, Cambridge, Mass.

Schmelzbach C., D. Sollberger, S. A. Greenhalgh, H. Horstmeyer, H. Maurer and J.O.A. Robertsson, 2016. 9C seismic data acquisition for near-surface applications: recording, wavefrom reciprocity and 4C rotation. 78th EAGE conference and exhibition. Extended abstract WS04 B03

SIA, 2014. SIA 261 Einwirkungen auf Tragwerke. Société Suisse des ingénieurs at des architectes, Zurich, Switzerland.

Socco, L.V., and C. Strobbia, 2004. Surface-wave method for near-surface characterization: a tutorial: Near Surface Geophysics, **2**, no. 4, 165-185.

Socco, L.V., D. Boiero, S. Foti, and R. Wisen, 2009. Laterally constrained inversion of ground roll from seismic reflection records: Geophysics, **74**, no. 6, G35-G45.

Sollberger D., C. Schmelzbach, C. Van Renterghem, J. O. Robertsson and S. A- Greenhalgh, 2016. Single-component elastic wavefield separation at the free surface using source- and receiver-side gradients. SEG International Exposition and 86th annual meeting, 2268 – 2273.

Swisstopo, Service géologique national, 2011. Atlas géologiques de la Suisse 1:25000 : LK 1048 feuille de Rheinfelden.

Swisstopo, Service géologique national, 2019. Digital bedrock elevation model in the Molasse Basin and the larger Alpine valleys. https://shop.swisstopo.admin.ch/en/products/geological_models/bedrock_elevation